Identification of magnetic enhancement at hydrocarbon-fluid contacts

Sijibomioluwa A. Badejo, Adrian R. Muxworthy, Alastair Fraser, Graham R. Stevenson, Xiang Zhao, and Michael Jackson

ABSTRACT

Identifying the depths of the hydrocarbon-fluid contacts in a reservoir is important for determining hydrocarbon reserves and production planning. Using core samples from the Tay Sandstone reservoir in the central North Sea, we show that there is a magnetic enhancement at the hydrocarbon-fluid contacts that is detectable through both magnetic susceptibility measurements and magnetic hysteresis measurements. We observed this magnetic enhancement at both gas-oil and oil-water contacts, which have been independently identified using nonmagnetic methods; we did not consider gas-water contacts in this study. We demonstrate that this magnetic enhancement is caused by the precipitation of new nanometric iron oxide (magnetite) and iron sulfide (greigite) phases. The magnetic enhancement may be caused by diagenetic changes or preferential biodegradation at the top of the oil column during early filling and at the oil-water contact. Our findings have the potential to be used to identify paleo-hydrocarbonfluid contact in both structurally modified fields and failed wells. The technique can also be used to infer the fill history of a basin and calibrate petroleum systems models. Magnetic susceptibility measurements have the advantage that they can easily and quickly be measured in the field on whole core material.

INTRODUCTION

Hydrocarbon-fluid contacts are boundaries that separate hydrocarbon phases from each other and from the formation water (Ahmed, 1989). Identifying the locations of these hydrocarbon-fluid contacts is crucial for determining hydrocarbon reserves and production planning.

As source rocks undergo burial, oil is generated and then expelled. The oil commonly migrates upward because of buoyancy,

Copyright ©2021. The American Association of Petroleum Geologists. All rights reserved.

Manuscript received September 5, 2019; provisional acceptance January 28, 2020; revised manuscript received June 2, 2020; final acceptance January 15, 2021.

DOI:10.1306/07062019207

AUTHORS

SIJIBOMIOLUWA A. BADEJO ~ Department of Earth Science and Engineering, Imperial College London, London, United Kingdom; present address: CGG, Tyn Y Coed, Llanrhos, Llandudno, United Kingdom; Sijibomioluwa.Badejo@CGG.com

Sijibomioluwa A. Badejo obtained a Ph.D. at Imperial College London and is now working for CGG.

ADRIAN R. MUXWORTHY ~ Department of Earth Science and Engineering, Imperial College London, London, United Kingdom; adrian.muxworthy@imperial.ac.uk

Adrian R. Muxworthy is the corresponding author and a reader in earth and planetary magnetism.

ALASTAIR FRASER ~ Department of Earth Science and Engineering, Imperial College London, London, United Kingdom; alastair. fraser@imperial.ac.uk

Alastair Fraser holds a Chair in Subsurface Geoscience, and has more than 30 years of industry experience with BP.

GRAHAM R. STEVENSON ~ Department of Earth Science and Engineering, Imperial College London, London, United Kingdom; q.stevenson15@imperial.ac.uk

Graham R. Stevenson completed his Ph.D. at Imperial College London in 2020.

XIANG ZHAO ~ Research School of Earth Sciences, Australian National University, Canberra, Australia; xiang.zhao@anu. edu.au

Xiang Zhao is a postdoctoral fellow at Australian National University, having gained his Ph.D. at the University of Southampton, United Kingdom.

MICHAEL JACKSON ~ Institute for Rock Magnetism (IRM), University of Minnesota, Minneapolis, Minnesota; xiang.zhao@anu. edu.au

Michael Jackson is emeritus facility manager at the IRM, having worked at the IRM for more than 25 years.

ACKNOWLEDGMENTS

This work was partly funded by Petroleum Technology Development Fund Nigeria, and a Visiting Fellowship to the IRM, University of Minnesota. The IRM is funded by the Instruments and Facilities program of the Earth Sciences Division of the National Science Foundation, and by the University of Minnesota. We thank Dana Petroleum for provision of the oil samples.

until it escapes at the surface or seabed or is trapped in a reservoir. As burial depth increases, depending on the kerogen type, the source rock can also expel gas, which also migrates upward but typically at faster rates than oil. If gas reaches the reservoir it will dissolve in the oil, potentially creating a multiphase system depending on pressure and temperature (Larter and di Primio, 2005). As pressure drops or temperature increases, the gas exsolves from the oil and a gas cap is formed above the oil with the formation water lying below the oil (Ahmed, 1989).

Resistivity wire-line logs (Figure 1) are good for identifying oil-water contacts (OWCs) and gas-water contacts (GWCs), because the resistivity of hydrocarbons is significantly higher than that of water (Rider and Kennedy, 1996). However, because oil and gas have roughly the same resistance, resistivity logs cannot be used to differentiate gas-oil contacts (GOCs). To identify GOCs (and GWCs), neutron porosity and density wire-line logs can be used; gas is less dense than oil or water. and because neutron-derived porosities for gas are significantly underestimated, this provides a clear contrast (known as the gas effect) as shown in Figure 1 (Rider and Kennedy, 1996). It has been found that hydrocarbon-fluid contacts are not always sharp boundaries; they can be gradational with an intermediate transition zone of mixed fluids. Depending on the lateral pressure, variation in the reservoir bed can be flat or tilted (Dennis et al., 2000). If pressure data (e.g., wireline repeat formation tester data) are available, an accurate determination of fluid contacts can be made.

The reducing conditions generated by hydrocarbons can alter (produce or destroy) the ferromagnetic minerals that may be present, that is, iron oxides and iron sulfides depending on the conditions (Reynolds et al., 1990; Emmerton et al., 2012; Abubakar et al., 2015, 2020). The iron oxide magnetite and the iron sulfides pyrrhotite and greigite are the most common magnetic minerals precipitated, whereas the iron oxide hematite, if initially present, typically gets replaced or dissolved. Also common in these environments are iron-rich nonmagnetic minerals such as pyrite and siderite (Machel, 1995). The exact balance of magnetic and nonmagnetic iron-rich minerals depends on the local environment.

Mineral magnetic measurements carried out on shallow drill cuttings from oil-producing and dry wells from oil fields in Venezuela have found magnetic susceptibility anomalies in oil-producing wells that are caused by the presence of iron-rich spherical aggregates and magnetic phases of authigenic origin (Costanzo-Alvarez et al., 2000; Aldana et al., 2003). Similarly, Liu et al. (2006) found that in addition to anomalies in the magnetic susceptibility, magnetic hysteresis parameters that are mass dependent (e.g., saturation magnetization $[M_s]$ and remanent saturation magnetization $[M_{rs}]$) were 2–5 times

higher in oil-producing zones compared to non–oil-producing zones with fine-grained (~25 nm) magnetite contributing to this enhanced signal. This enhanced signal in the oil-bearing layers has also been attributed to the presence of fine-grained pyrrhotite in oil wells located in Venezuela and Oklahoma (Reynolds et al., 1990; Mena and Walther, 2012).

We have identified a magnetic enhancement at hydrocarbon-fluid contacts. In this paper, we show that peaks in magnetic susceptibility, M_s , and remanent saturation, coupled with size of magnetic minerals, can be used to determine the hydrocarbon contacts on core samples. These new approaches have the potential to be used in the identification of paleo-hydrocarbon-fluid contacts, which are vital to understanding the fill history of basins. To demonstrate these effects, we have obtained and studied core samples from the Tay Sandstone Member in the Central North Sea Basin.

STUDY AREA

The wells used in this study are in the Central North Sea Basin of the United Kingdom North Sea (Figure 2). The central graben is located approximately 240 km east of Scotland and is one of the three arms of the failed North Sea rift system, which also includes the Viking graben and the Inner and Outer Moray Firth (Erratt et al., 1999).

A stratigraphic column of the study area is shown in Figure 3. The Upper Jurassic Kimmeridge Clay is the main source rock in the area (Figure 3). It is mature for oil to the east of the study area, with burial depths greater than 3250 m, and generally late mature for oil to early mature for gas at the eastern edge, with burial depths of approximately 4750 m (Isaksen, 2004). In the central graben, the main hydrocarbon reservoirs are Upper Jurassic shallow marine sandstones and Cenozoic deep-water sandstones.

Initial accumulation of oil was in the Upper Jurassic Fulmar Formation sandstones. Because the source rock lies directly above this formation, it makes an ideal short distance migration pathway. However, the Fulmar is affected by both stratigraphic complexity and salt movement, which makes sandstones commonly discontinuous and fractured. Over time, sediment loading led to capillary failure in the seal above the Fulmar sandstones, which initiated

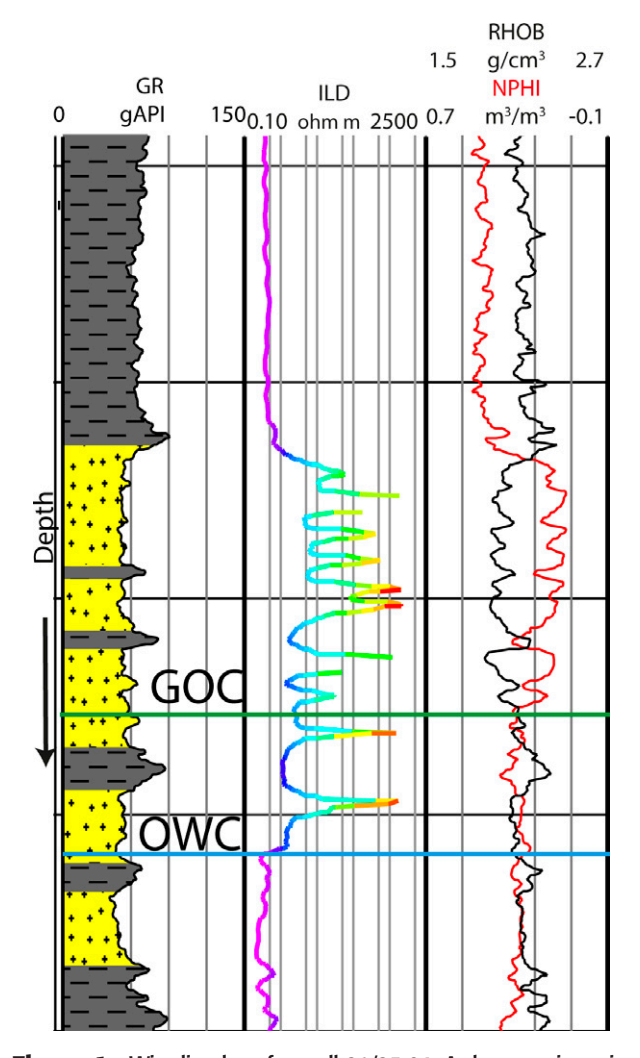


Figure 1. Wire-line logs for well 21/25-04. A decrease in resistivity indicates a change from hydrocarbons to formation water. GOC = gas-oil contact; GR = gamma-ray log; ILD = deep induction log used to determine formation resistivity; NPHI = neutron porosity log; OWC = oil-water contact; RHOB = bulk density log.

vertical migration, with the fractured chalk and possibly the salt wall and diapirs acting as vertical conduits for migration into the overlying Cenozoic sandstones. In our study area, three-dimensional basin modeling (Badejo et al., in press) suggests the oil migrates vertically to the Tay Sandstone Member of Eocene age in the east and moves laterally to the west by a fill and spill mechanism. All the core samples studied are from this formation.

Compared to the Fulmar sandstones the Cenozoic sandstones are only slightly deformed and laterally continuous, facilitating lateral migration of distances of up to 50 km for oil and up to 32 km for gas (Cayley, 1987; Kubala et al., 2003).

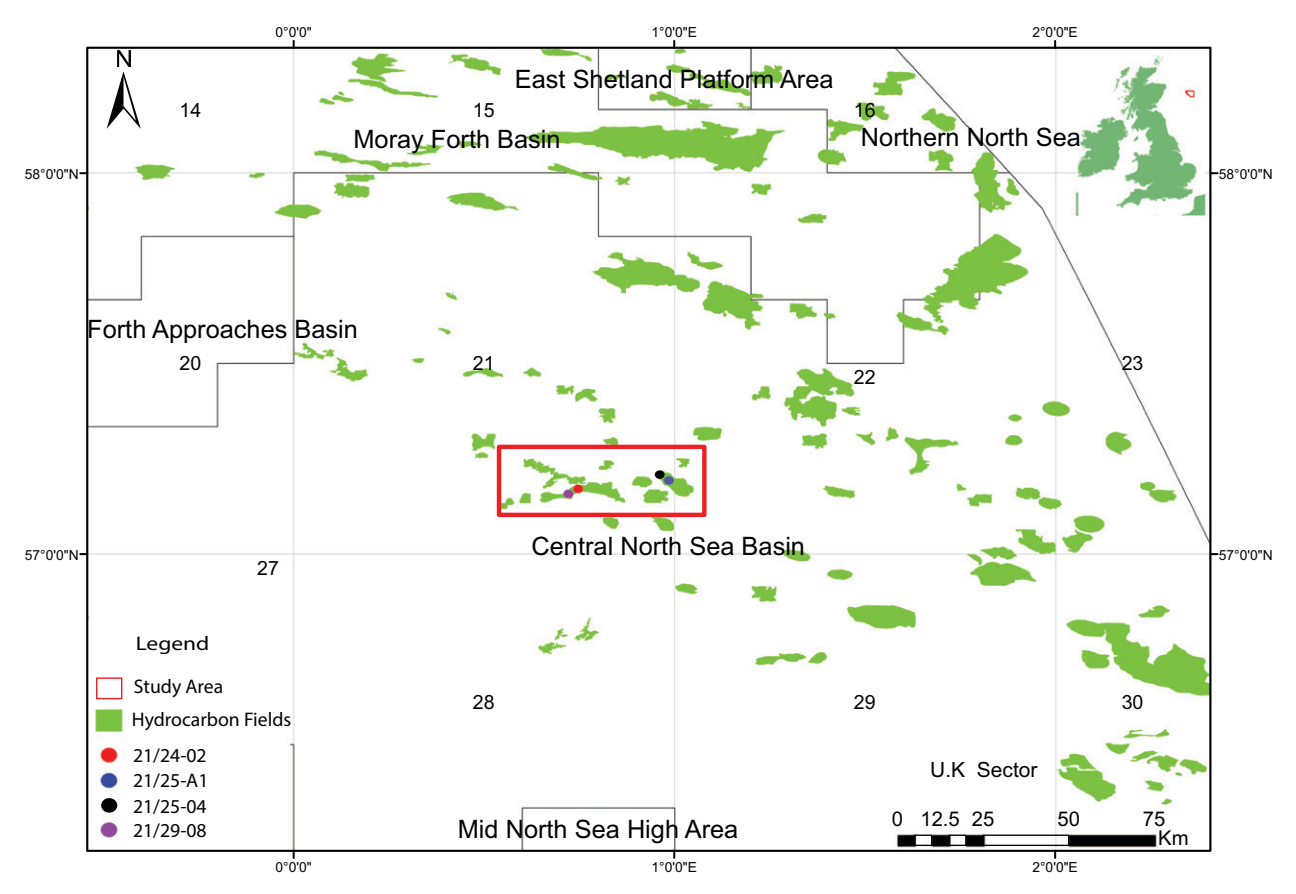


Figure 2. Study area (red rectangle) located in the western central graben of the United Kingdom North Sea. Known hydrocarbon fields are highlighted in green.

METHODOLOGY

Sample Collection

Well cores were sampled from the British Geological Survey core repository in Keyworth, United Kingdom. Composite logs were used to determine which wells in the study area have penetrated OWCs or GOCs or both: 6 out of the 18 wells selected have core material with a clear OWC, whereas only 2 wells sample a clear GOC. The composite logs were also used to determine the presence of hydrocarbon in the Tay Sandstone Member and if the core recovery was successful from the formation. Samples were selected based on geological observation (water-wet sandstone, oil-stained sandstone, sandstones in gas cap, siltstones, and shale). Samples taken were typically 2-cm chips. Data from wells 21/25-04, 21/25-A1, and 21/29a-08 are shown in this paper.

In addition to the core sections, pure oil samples were obtained from wells 21/29a-8 and 21/24-2 (Figure 2). The oil samples were absorbed in kaolinite clay for magnetic measurements. To purify the kaolinite clay, it was washed in hydrogen peroxide to get rid of any organic matter, then it was washed in deionized water and left in an oven at 100° C for 24 hr. For each sample, the mass of the kaolinite clay was measured before (1.98 g per sample) and after oil was added (\sim 3 g). Approximately 0.15 g of the mixture was used for the low-temperature (LT) experiments. The concentration of oil in both samples was \sim 35% by total mass; we subtracted that from the overall signal.

Magnetic Measurements

Magnetic measurements were carried out to determine the morphology, mineralogy, and size of the magnetic minerals present. The magnetic techniques used are described below.

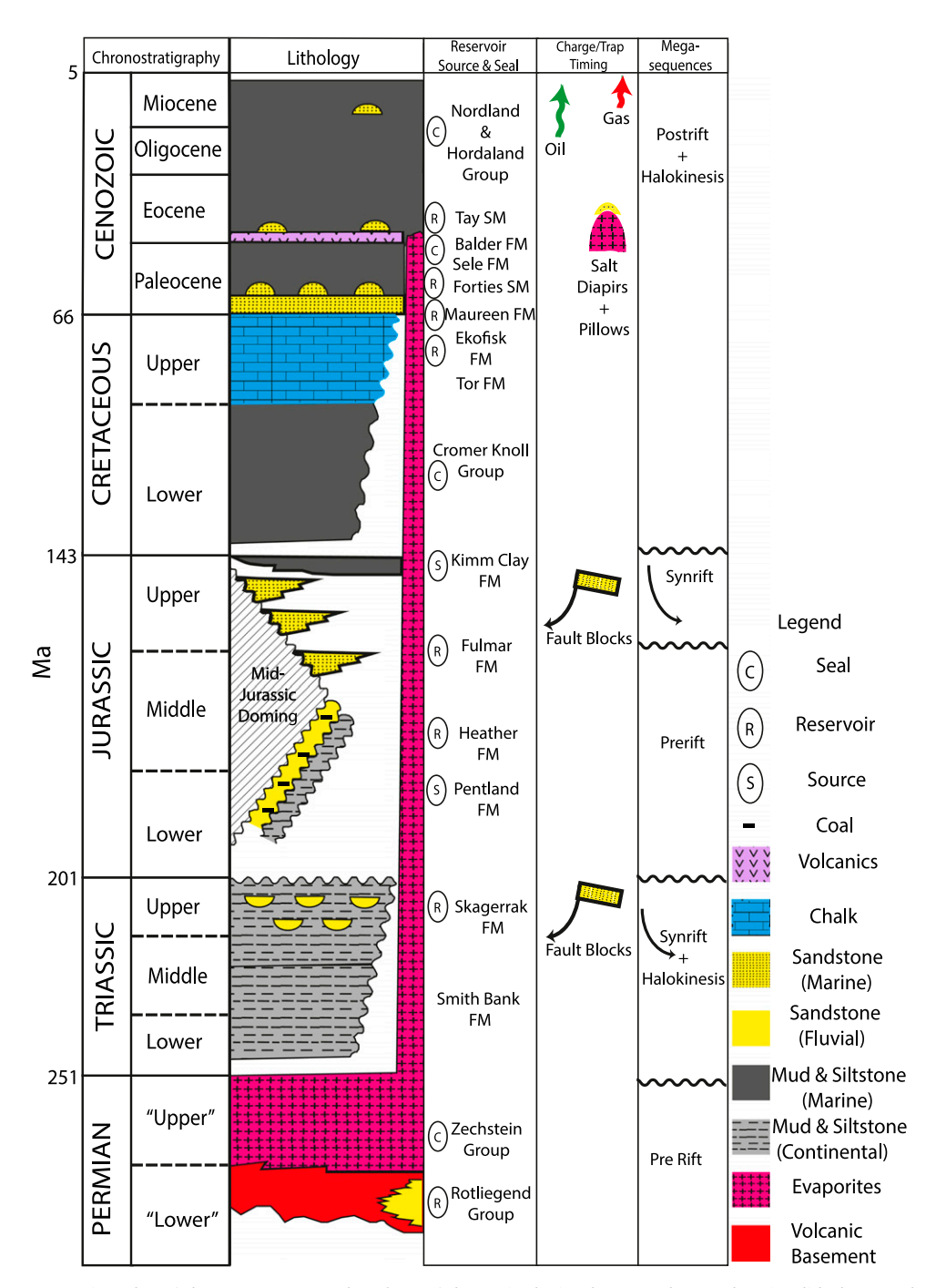


Figure 3. Tectonostratigraphy of the western central graben of the United Kingdom North Sea showing lithology and ages of rifting in the study area. FM = Formation; Kimm clay = Kimmeridge Clay; SM = Sandstone Member.

Magnetic Hysteresis Measurements

Room-temperature magnetic hysteresis measurements on a vibrating sample magnetometer (VSM) were done at Imperial College London. The VSM measures the magnetic response to an applied field. All materials fall into one of the three magnetic categories: diamagnetic, paramagnetic, or ferromagnetic. Diamagnetic and paramagnetic

minerals have a linear relationship with the applied field, with negative and positive slopes, respectively (Dunlop and Özdemir, 1997). In ferromagnetic materials, the magnetization does not return to zero when the field is removed but retains a record of the applied field. The path of magnetization as a function of the applied field is known as a hysteresis loop. If the applied field

reaches a sufficient level, the material acquires its M_s . Removing this field gives an M_{rs} . To reduce the magnetization to zero a reverse field, coercive force is applied.

In very small grains, the magnetization is uniform, and the particle is said to be single domain (SD) (Dunlop and Özdemir, 1997). As a grain gets bigger, its magnetization breaks up into areas (domains) of uniform magnetization separated by narrow domain walls; such grains are termed multidomain (MD). Small SD grains have magnetic moments that are unstable because of thermal fluctuations (<30 nm for magnetite), and are called superparamagnetic (SP) grains or thermally relaxing SD grains (Dunlop and Özdemir, 1997). Small MD grains just above the SD to MD threshold size (~100 nm for magnetite), display SD-like characteristics and are termed pseudosingle domain grain (PSD) (Roberts et al., 2017).

First-order reversal curves (FORC) diagrams are used to identify the domain state distributions within a sample (Roberts et al., 2000, 2014). A FORC diagram is calculated from a class of partial hysteresis curves (Roberts et al., 2000). As a first approximation, the x-axis represents the coercivity, whereas the y-axis describes the magnetic interaction within the sample. The "irregular" measurement protocol by Zhao et al. (2015) was used for all the FORCs in this paper.

LT Measurements

The LT (20–300 K) experiments were carried out on the Magnetic Properties Measurement System at the University of Minnesota's Institute for Rock Magnetism in Minneapolis. These measurements assist identification of the magnetic minerals present based on mineral-specific crystallographic transitions (e.g., the Verwey transition in magnetite at $T_V \sim 120$ K) (Verwey, 1939), the Morin transition in hematite at $T_M \sim 263$ K (Morin, 1950), the Besnus transition in monoclinic pyrrhotite at $T_{Bes} \sim 30$ –34 K (Besnus and Meyer, 1964), and to identify nanometric particles (<30 nm) that are difficult to detect at room temperature because of high thermal energy.

Susceptibility Measurements

High-temperature (HT) experiments were carried out on a KLY-2 KappaBridge AC Susceptibility Bridge in Imperial College London. Susceptibility was measured as samples were heated from room temperature to 700°C in an argon atmosphere. This is used to help determine the mineralogy of the samples based on their Curie temperature and thermomagnetic behavior (Dunlop and Özdemir, 1997).

A variable field susceptibility meter was used to measure the magnetic susceptibility at room temperature over a wide range of frequencies (30–10 kHz) at a field of 300 Am⁻¹ at Imperial College London. For small grains, susceptibility varies as a function of frequency because the grains behave as SP grains at low frequency and behave as SD grains at high frequency; larger grains (i.e., >40 nm) are essentially invariant to the applied frequencies (Muxworthy, 2001).

Scanning Electron Microscopy

Because the abundance of magnetic minerals was less than 1% of the sample, magnetic extraction was needed for imaging. Samples were crushed to an even grain size and passed through a Frantz electromagnet magnetic separator three times to reduce the abundance of nonmagnetic materials.

Samples were grounded and coated in gold for imaging energy-dispersive x-ray (EDX) analysis on the Zeiss LEO Gemini 1525 scanning electron microscope (SEM) at Imperial College London. The EDX analysis had a spot size of approximately 1 μ m. Some uncoated samples were also imaged on a Phenom desktop SEM.

RESULTS

Oil Samples

The following LT experiments were carried out on the samples to identify possible magnetic transitions. (1) LT demagnetization: the samples were induced with a saturation isothermal remanent magnetization (SIRM) at room temperature (RTSIRM; field = 2.5 T), and then cooled to 10 K and back to 300 K in zero-field. This generates two curves called RTSIRM cooling and RTSIRM warming curves. (2) Field-cooled (FC) – zero-field-cooled (ZFC) warming curves: induce a SIRM at 10 K and warm in zero field to 300 K. In the ZFC scenario, the sample is first cooled to 10 K in zero field; in the FC scenario, it is cooled in a field at 2.5 T. The RTSIRM cooling and warming and FC and ZFC curves were measured for the blank kaolinite clay and for the oil from wells 21/

24-02 and 21/29a-08 (Figure 4). The curves for the blank kaolinite clay (Figure 4A) are noisy and show no evidence for any magnetic minerals. In comparison, the signal-to-noise ratio for the oil samples (Figure 4B, C) is much higher (i.e., magnetization is approximately two orders of magnitude stronger).

Drops in remanence at approximately 120 K on the RTSIRM cooling curve suggest the presence of magnetite in both wells (Figure 4B, C), whereas a drop in magnetization at approximately 37 K on the cycling cooling curve (Figure 4B) could be caused by the presence of monoclinic pyrrhotite in well 21/24-02 (Verwey, 1939; Besnus and Meyer, 1964).

Core Samples

Hysteresis loops (Figure 5), FORC diagrams (measured if signal-to-noise ratio in the loop was high enough), and susceptibility were measured for all samples. An increase in M_s , M_{rs} , and susceptibility (normalized by mass) were noticed at the hydrocarbon-fluid contacts as shown in wells 21/25-04, 21/25-A1, and 21/29a-08 (Figure 6). Differences

in susceptibility measured at 990 Hz and 6000 Hz observed in samples from well 21/25-A1 and 21/25-04 (Figure 6D, E) suggest the presence of SP grains (i.e., 25–35 nm in size) (Muxworthy, 2001; Mena and Walther, 2012).

The LT experiments identified the presence of magnetite (decrease in remanence at ~120 K) in all the samples (Figures 7, 8). The increase in remanence on cooling noticed in most of the samples (e.g., s63594, s63600, s73397, and s72399) (Figures 7A, M and 8D, G, respectively) suggests the presence of goethite or titanohematite (Sprain et al., 2016). The RTSIRM cooling and warming curves identified the presence of hematite (drop in remanence at ~250 K) in a few samples (e.g., s63599) (Figure 7J). This was expected because hematite is commonly replaced or dissolved in diagenetic settings caused by hydrocarbons (Burton et al., 1993).

No Besnus transition was noticed in any of the LT curves measured, indicating there is no monoclinic pyrrhotite in the samples, but other iron sulfides such as hexagonal pyrrhotite or greigite may be present because they have no LT transition (Horng,

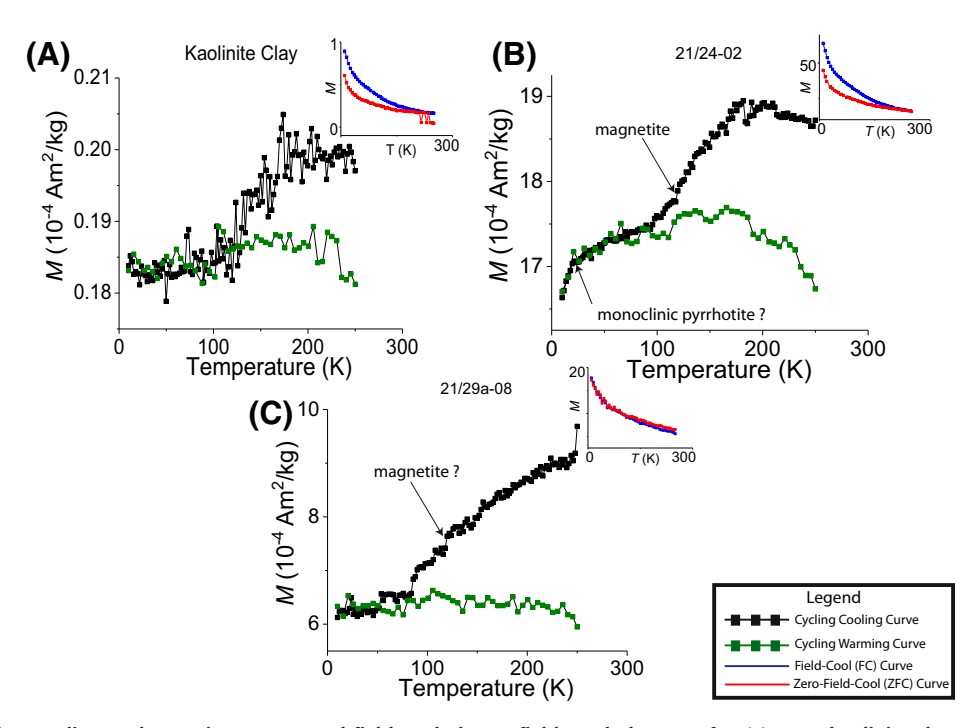


Figure 4. Cycling cooling and warming curves and field-cooled zero-field-cooled curves for (1) pure kaolinite clay-noisy signal; (2) oil sample from well 21/24-02: cycling and warming curves suggest the presence of magnetite and possibly monoclinic pyrrhotite in the sample; (3) oil sample from well 21/29a-08: cycling cooling and warming curves suggest the presence of magnetite in the sample. M = magnetization.

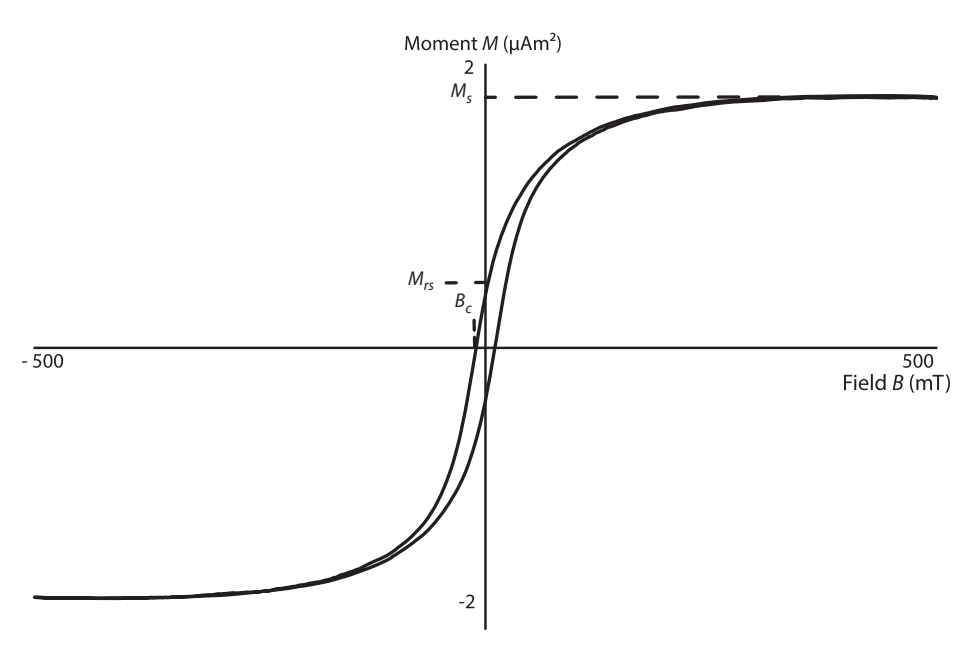


Figure 5. Hysteresis loop of sample s63654 from well 21/25-04 annotating saturation magnetization (M_s), remanent saturation magnetization (M_s), and coercivity (B_c).

2018). The absence of a lambda transition (rapid increase in susceptibility at ~200°C followed by a rapid decrease in susceptibility at 250°C) in the HT-susceptibility experiments suggests a lack of hexagonal pyrrhotite in the samples (Dunlop and Ozdemir, 1997). Greigite is typically unstable during heating with thermal decomposition 200°C-400°C (Chang et al., 2008). Its presence in samples is inferred from the HT-susceptibility heating and cooling behaviors; kinks in susceptibility on heating between 200°C and 400°C (e.g., s72399, s7203, and s72406) (Figures 8H, K, and N, respectively) have been attributed to the presence of greigite (Dekkers et al., 2000).

Siderite is paramagnetic at room temperature, but in the presence of a field it acquires a large thermal remanence on cooling below its Néel temperature (~37 K) (Frederichs et al., 2003). On heating of LT SIRM after FC or ZFC, there is a noticeable drop in remanence between 10 and 40 K in the FC experiment. This was used to identify the presence of siderite as shown in samples s63599 and s72399 (Figures 7J, 8G). In the absence of FC and ZFC curves, the heating and cooling behavior of susceptibility was used to identify siderite. When heating in argon, siderite alters to magnetite above 400°C, and on cooling, a rapid increase in susceptibility at 580°C

accompanied by a Hopkinson-like peak is observed, suggesting the formation of SP magnetite (Housen et al., 1996). This behavior was noticed in samples s63594, s63596, s63598, s63599, s63600, s72396, s72397, s72399, and s72403 (Figures 7B, E, H, K, N; 8B, E, H, K).

The FORC diagrams with a vertical spread of concentric contoured peaks on the vertical axis $B_i = 0$ suggest the presence of interacting SD particles (Roberts et al., 2000). Such behavior is observed at the hydrocarbon-fluid contacts seen in s63594 and s63599 (Figure 7F, I). The FORC diagrams with a contoured peak below the $B_i = 0$ axis are indicative of SD greigite (Horng, 2018); this was observed in one well 21/25-A1 at the OWC (sample s72403; Figure 8L). The FORC diagrams for some samples have a vertical spread on the B_i axis, which suggests the presence of PSD grains (Roberts et al., 2000, Roberts et al., 2017) as seen in s63594, s63596, and s63598 (Figure 7C, F, I). The FORC diagrams also suggest the presence of SP grains (Roberts et al., 2018) above and below the hydrocarbon-fluid contact as seen in samples s63594, s63598, s63600, s72396, s72399, and s72406 (Figures 7C, I, O; Figures 8C, I, O). Samples with multiaxial anisotropy were identified by the steeply dipping negative region to the right of the horizontal B_u axis (Valdez-Grijalva and Muxworthy,

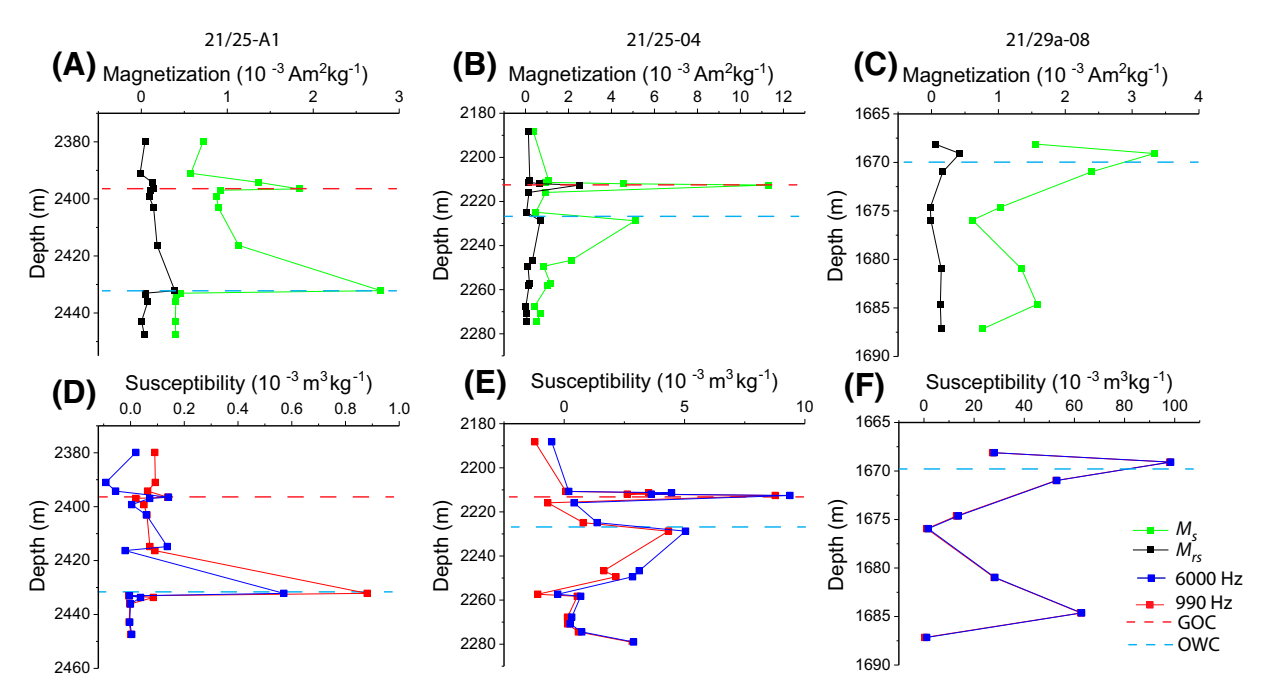


Figure 6. Saturation magnetization (M_s ; green line), remanent saturation magnetization (M_{rs} ; black line), susceptibility measured at 990 Hz (red line), and 6000 Hz (blue line) for samples from wells 21/25-A1 (A and D), 21/25-04 (B and E), and 21/29a-09 (C and F). Distinct peaks are noticed at the gas-oil contact (GOC) (red dashed line) and oil-water contact (OWC) (blue dashed line). The GOC and OWC depths were obtained from wire-line logs. All depths are below mean sea level.

2019) (Figures 7C, F, I; Figure 8C, F, I, L, O). This feature may also be because of SD vortex behavior (Lascu et al., 2018; Valdez-Grijalva et al., 2018).

The SEM images on magnetic extracts showed a variety of grain sizes and iron-phase mineralogy. Framboids were found in samples such as s63598 (Figure 9A). The EDX analysis of the framboid in Figure 9 identified iron- and sulfur-containing grains, which are likely (the EDX was not calibrated for this) a mixture of 1–2-μm-sized pyrite grains and smaller-than-100-nm greigite grains. Bigger magnetite and pyrite grains (3–5-μm-sized) were found as well (e.g., s63597) (Figure 9B); the bigger magnetite grains are likely responsible for the PSD behavior noticed in s63594, s63596, and s63598 (Figure 7C, F, I). The EDX confirmed the presence of iron oxide minerals, which are most likely magnetite grains ranging from 50 to 350 nm in size (Figure 9C, D).

DISCUSSION

Peaks in M_s , M_{rs} , and susceptibility have been found at the hydrocarbon-fluid contacts (Figure 6). The hysteresis parameters have been "slope corrected,"

(i.e., linear diamagnetic and paramagnetic contributions removed); however, the susceptibility measures the total magnetic signal, which possibly includes contributions from Fe-bearing paramagnetic minerals that are common in, for example, clays. The behavior at the OWC appears clear, and there is an enhancement in both the hysteresis (ferromagnetic) signal and the susceptibility (ferromagnetic and paramagnetic). At the GOC, there is an enhancement in the ferromagnetic signal, but in Figure 6D, it is seen that the combined paramagnetic and ferromagnetic signal is invariant to the GOC. We suggest that the ferromagnetic minerals at this GOC are forming at the expense of the paramagnetic signal (i.e., iron-rich paramagnetic minerals are becoming ferromagnetic).

The FORC diagrams from samples at the hydrocarbon-fluid contacts (Figures 7F, L and 8L, respectively) suggest the presence of stable SD grains (i.e., ~50–100 nm). The FORC diagrams from samples above and below the hydrocarbon contacts suggest the presence of smaller SP grains and PSD grains (Figures 7C, I, O; 8C, I, O). The LT and HT experiments confirmed the presence of magnetite, greigite, siderite, hematite, titanohematite, and goethite in the samples (Figures 7, 8). Only magnetite was

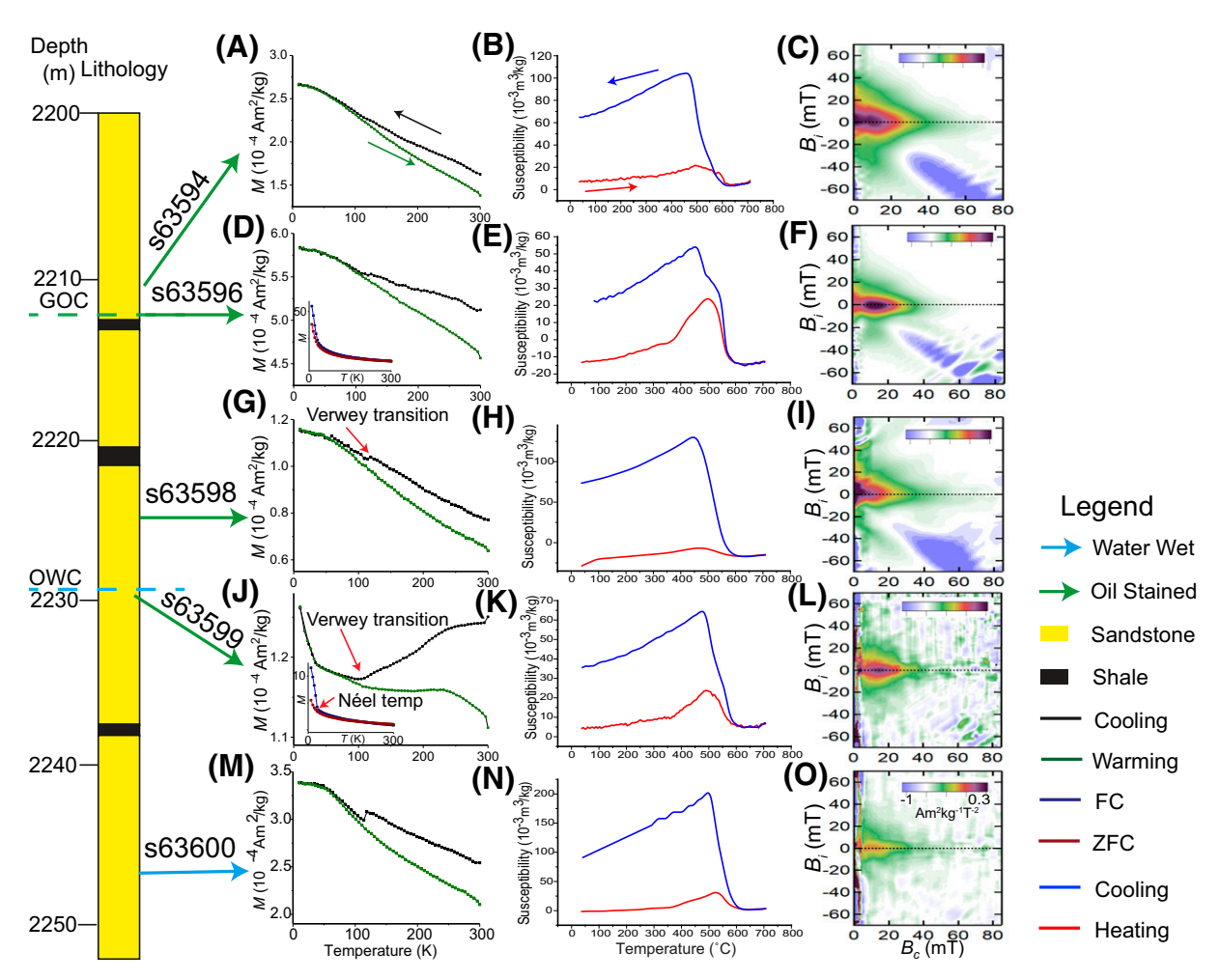


Figure 7. Low-temperature (LT) experiments (cycling cooling, cycling warming, field-cooled [FC], and zero-field-cooled [ZFC]), high-temperature (HT), susceptibility experiments, and first-order reversal curve (FORC) diagrams for samples in well 21/25-04. S63594: (A) LT experiments suggest the presence of titanohematite or goethite and magnetite, (B) HT experiment suggests a siderite-rich sample, and (C) FORC diagram suggests a mixture of superparamagnetic (SP) grains with multiaxial anisotropy or a vortex structure and pseudosingle-domain (PSD) grains. S63596 at the gas-oil contact (GOC): (D) LT experiments suggest the presence of titanohematite or goethite and magnetite, (E) HT experiment suggests a siderite-rich sample with some iron sulfides, and (F) FORC diagram suggests a mixture of single-domain (SD) grains with multiaxial anisotropy or vortex structure and PSD grains. S63598: (G) LT experiments suggest the presence of titanohematite or goethite and magnetite, (H) HT experiment suggests a siderite-rich sample, and (I) FORC diagram suggests a mixture of SP grains with multiaxial anisotropy or a vortex structure and PSD grains. S63599 at the oil-water contact (OWC): (J) LT experiments suggest the presence of hematite, siderite, and magnetite; (K) HT experiment suggests a siderite-rich sample; and (L) FORC diagram suggests the presence of SD grains. S63600: (M) LT experiments suggest the presence of SP grains. The VARIFORC parameters (Egli, 2013) for FORC smoothing are $s_{c0} = 1.2$, $s_{c1} = 3$, $s_{b0} = 3$, $s_{b1} = 5$, and $λ_c = 1$, $λ_b = 1$. Samples were heated in argon. M = magnetization.

observed in the oil-well samples, with possibly monoclinic pyrrhotite also present.

Can Magnetic Minerals Be Carried in the Oil?

The oil samples from wells 21/24-02 and 21/29a-08 (Figure 5B, C) have magnetizations that are two orders of magnitude higher than the kaolinite clay

sample (Figure 5A) and contain magnetite (identified by its Verwey transition at ~ 120 K). This suggests the magnetic minerals can form complexes within the oil that can be transported from the source rock to the reservoir provided they are small enough to fit through the pore throats of the carrier beds. The presence of framboids (e.g., s63597) (Figure 9A) suggests the diagenetic conditions caused by the oil could lead to the

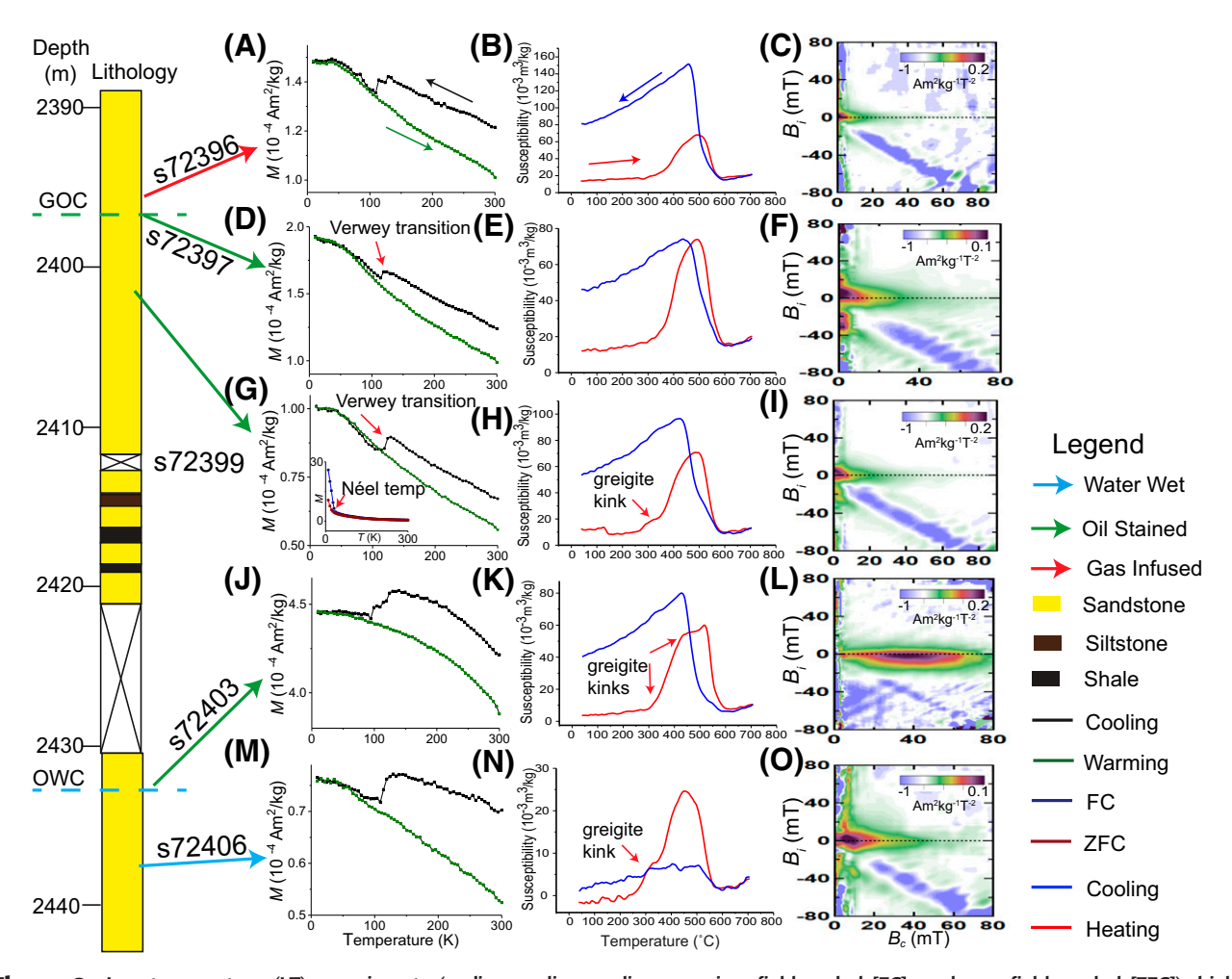


Figure 8. Low-temperature (LT) experiments (cycling cooling, cycling warming, field-cooled [FC], and zero-field–cooled [ZFC]), high-temperature (HT) susceptibility experiments, and first-order reversal curve (FORC) diagrams for samples in well 21/25-A1. S72396: (A) LT experiments suggest the presence of titanohematite or goethite and magnetite, (B) HT experiment suggests a siderite-rich sample, and (C) FORC diagram suggests the presence of superparamagnetic (SP) grains with multiaxial anisotropy or a vortex structure. S72397 at the gasoil contact (GOC): (D) LT experiments suggest the presence of titanohematite or goethite and magnetite, (E) HT experiment suggests a mixture of siderite and iron sulfides, and (F) FORC diagram suggests a mixture of SP and single-domain (SD) grains with multiaxial anisotropy or vortex structure. S72399: (G) LT experiments suggest the presence of titanohematite or goethite, siderite, and magnetite, (H) HT experiment suggests the presence of siderite and iron sulfides, and (I) FORC diagram suggests the presence of SP grains with multiaxial anisotropy or vortex structure. S72403 at the oil-water contact (OWC): (J) LT experiments suggest the presence of titanohematite or goethite and magnetite, (K) HT experiment suggests the presence of siderite and iron sulfides, and (L) FORC diagram suggests the presence of SD greigite grains. S72406: (M) LT experiments suggest the presence of SP grains. The VARIFORC parameters (Egli, 2013) for FORC smoothing are $s_{c,0} = 1.2$, $s_{c,1} = 3$, $s_{b,0} = 3$, $s_{b,1} = 5$, and $\lambda_c = 1$, $\lambda_b = 1$. Samples were heated in argon. M = magnetization.

precipitation of magnetic and nonmagnetic minerals in the reservoir that are too large to be transported (Wilkin and Barnes, 1997; Lin et al., 2016).

The drop in remanence at ~ 37 K on the cycling cooling curve in oil sample 21/24-02 (Figure 5B) is typically indicative of monoclinic pyrrhotite, but the ZFC and FC curves (insert in Figure 4B) do not support this argument (Kind et al., 2013). Additionally,

monoclinic pyrrhotite was not observed under the SEM in any of the measured core samples. It is commonly considered to be detrital in origin because it is thought to grow too slowly in sediments to be a diagenetic product (Roberts, 2015; Horng and Roberts, 2018). Monoclinic pyrrhotite is therefore unlikely to be the cause of the reduction in remanence observed at approximately 37 K in oil sample 21/24-02

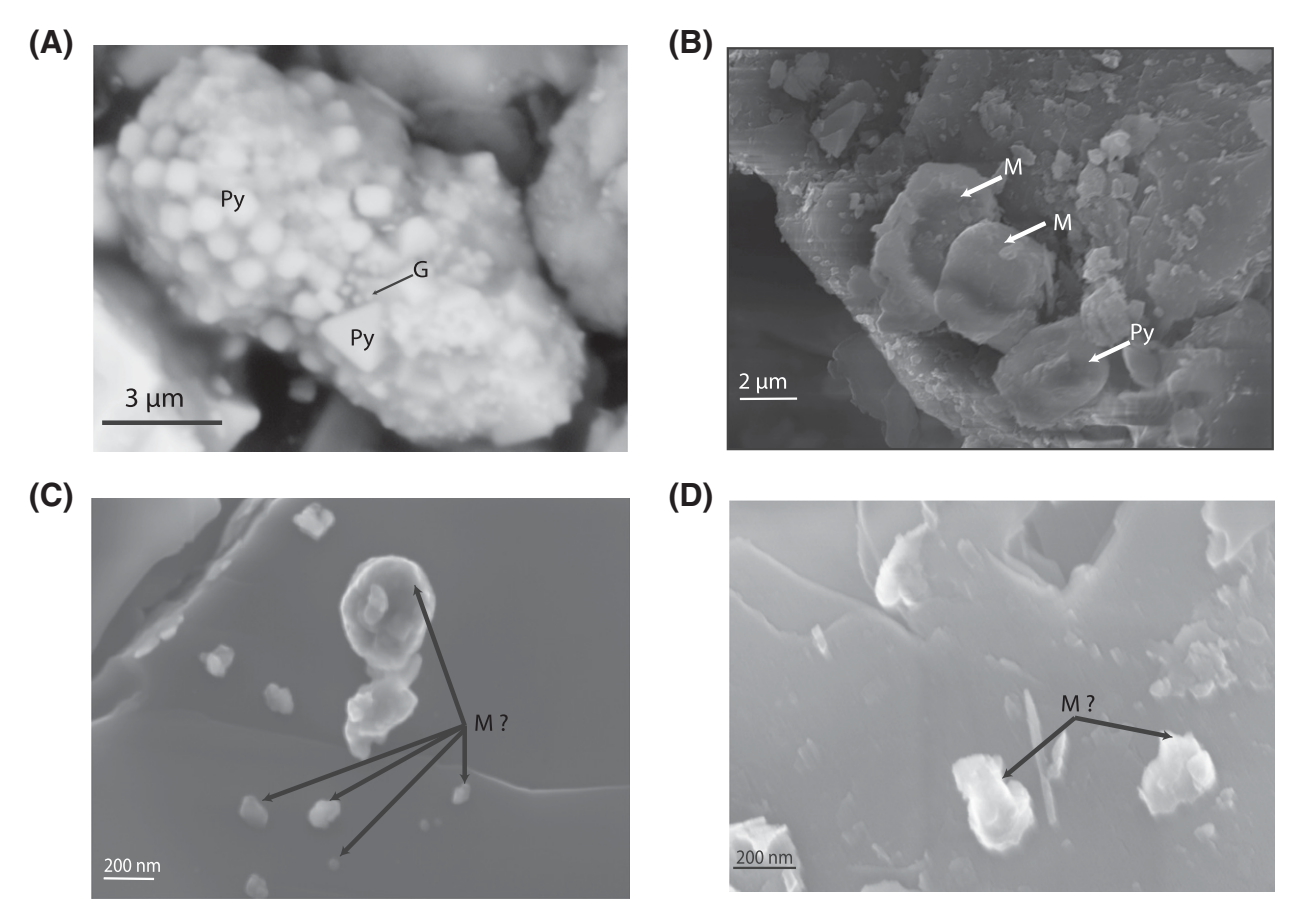


Figure 9. Scanning electron microscopy (SEM) images on the Phenom desktop SEM (A) s63597 energy-dispersive x-ray analysis confirms FeS Framboid. The SEM images on the LEO SEM; (B) and (C) s63598 from well 21/25-04, and (D) s63600 from well 21/25-04. G = greigite; M = magnetite, Py = pyrite.

(RTSIRM cooling curve in Figure 5B). It is unclear which mineral is responsible for this.

Surprisingly there was no evidence for siderite in any of the measurements from the two oil samples (Figure 5), although it was found in the core samples (e.g., s63599) (Figure 7J). Siderite is typically authigenic in origin and has been observed in hydrocarbon reducing environments (Burton et al., 1993; Machel, 1995; Emmerton et al., 2012; Roberts, 2015). It is possible that siderite is precipitated in the reservoir and the grains are bigger than the minimum pore throat of sandstone (2 μ m) or it acts as a cementing agent (Nelson, 2009; Roberts, 2015). Therefore, it is not extracted along with the oil.

Are the Magnetic Minerals Authigenic or Detrital or Do They Migrate?

Abubakar et al. (2015) showed that magnetic minerals are formed in situ in a mature source rock. They concluded that the vast majority of these minerals

were <60 nm and have the potential to be transported, although this may have been a result of the length of the duration lab experiments; in nature, the minerals might be larger.

The magnetic minerals in the core samples are likely a mixture of authigenic, detrital, and transported from source rock (Kimmeridge Clay) minerals. It is difficult to determine to which of these categories the magnetic minerals in the core samples belong. The source rock in this area is a mudstone (Kimmeridge Clay), which typically has pore-throat sizes ranging from 5 nm to 100 nm, whereas the sandstone reservoir typically has 2–20um pore-throat sizes (Nealson, 2009). Magnetic minerals that migrate with the oil from the source rock must be less than 100 nm because the oil also passes through layers of shale. This suggests that the <100-nm grains that are responsible for the SP and SD FORC signatures observed in our samples (e.g., s63596, s72396, and s72403) (Figures 7F;

8C, L) could have been transported from the source rock, whereas the >150-nm grains are either detrital or authigenic. The framboids, pyrite, and siderite are authigenic, whereas the >1-μm magnetite grains and titanohematite are most likely detrital or as a result of drilling mud contamination. Similar observations have been made by Liu et al. (2006).

There is also the possibility that the measured magnetic response is caused by chemical alteration of iron-rich phases during the 20–30 yr the cores have been stored, however, we deem this unlikely as the enhanced response is seen in several wells in multiple samples.

Unraveling the Magnetic Signature: End-Member Analysis

For two of the wells in the area, the FORC diagrams were analyzed using principal component analysis (PCA) to help understand variance in FORC distributions as a function of depth and to help identify possible end members (EMs) (Harrison et al. (2018). To do this we used version 3.06 of the FORCinel software package (Harrison and Feinberg, 2008).

Ten samples from well 21/25-04 (Figure 7) were selected for FORC-PCA, and 95% of the variance was defined by two EMs: EM1 accounted for 90% of the variance whereas EM2 accounts for 5% of the variance. The data are plotted in the principal component plane in Figure 10A. The two components identified (Figure 10B, C) are represented by SP particles (EM1) and SD particles with multiaxial anisotropy or vortex behavior (EM2). The PSD behavior is observed in both EMs. The depth variation of the two components identified is shown in Figure 10D. The FORC-PCA for well 21/25-04 (Figure 10D) showed a noticeable increase in the proportion of SD particles (EM2) at the GOC and OWC. This is also accompanied by a reduction in the proportion of SP particles (EM1) at the GOC and an increase in proportion of EM1 at the OWC.

A new FORC-PCA was carried out on 12 samples in well 21/25-A1, and the variance in the data were defined by three newly defined EMs (Figure 11A): EM1 accounts for 50% of the variance, whereas EM2 accounts for 45% and EM3 accounts for 2%. The three components identified (Figure 11B–D) are represented by SP particles (EM1), SP particles with multiaxial anisotropy or vortex

behavior (EM2), and stable SD greigite particles (EM3). The proportions of these EMs are shown in Figure 11E. Peaks in the proportions of EM3 are found at the OWC and GOC (Figure 11E). The proportion of EM1 and EM2 decreases at the OWC. At the GOC, a drop in EM1 is accompanied by an increase in EM2. The EM1 is more prominent below the GOC and OWC.

These SD grains identified at the hydrocarbon contacts can be either magnetite as seen in well 21/ 25-04 (EM2, Figure 10) or greigite as seen in well 21/25-A1 (EM3, Figure 11). The FORC-PCA aids in the interpretation of the data because it was able to pick out trends that go unnoticed in FORC diagrams if they were just compared by mere observation. For example, the FORC diagram at the GOC for well 21/25-A1 showed no SD signal (Figure 8F), but the PCA was able to identify a relative increase in SD particle proportions at the GOC (Figure 11). The proportion of these SD particles is roughly correlated with the M_s , M_{rs} , and susceptibility; the highest M_s , M_{rs} , and susceptibility values are noticed at the GOC in well 21/25-04 (Figure 6B, E). This also corresponds to the maximum proportion of SD particles (Figure 10D) and is consistent with the highest M_{s} , M_{rs} , and susceptibility values measured at the OWC in well 21/25-A1 (Figure 6A, D), again showing the highest SD proportions (Figure 11E).

Magnetic Enhancement at the Hydrocarbon-Fluid Contacts

The FORC-PCA demonstrated the increased abundance of stable SD material at the GOC and OWC (Figures 10D, 11E). This increased abundance of larger SD grains at the hydrocarbon-fluid contacts is most likely caused by changes in diagenetic conditions. Here, we discuss two possible mechanisms for the enhancement: (1) thermodynamic and (2) biological.

First, a thermodynamic model: Burton et al. (1993) calculated thermodynamic stability diagrams for iron-bearing minerals at temperatures (50–200°C) and pressures (1–600 bar) similar to those expected in our reservoirs. All the minerals identified in our samples are represented in the thermodynamic stability diagrams of Burton et al. (1993), apart from greigite (Figure 8L); at the time, the importance of greigite was not appreciated and was not included in their models. It is now thought

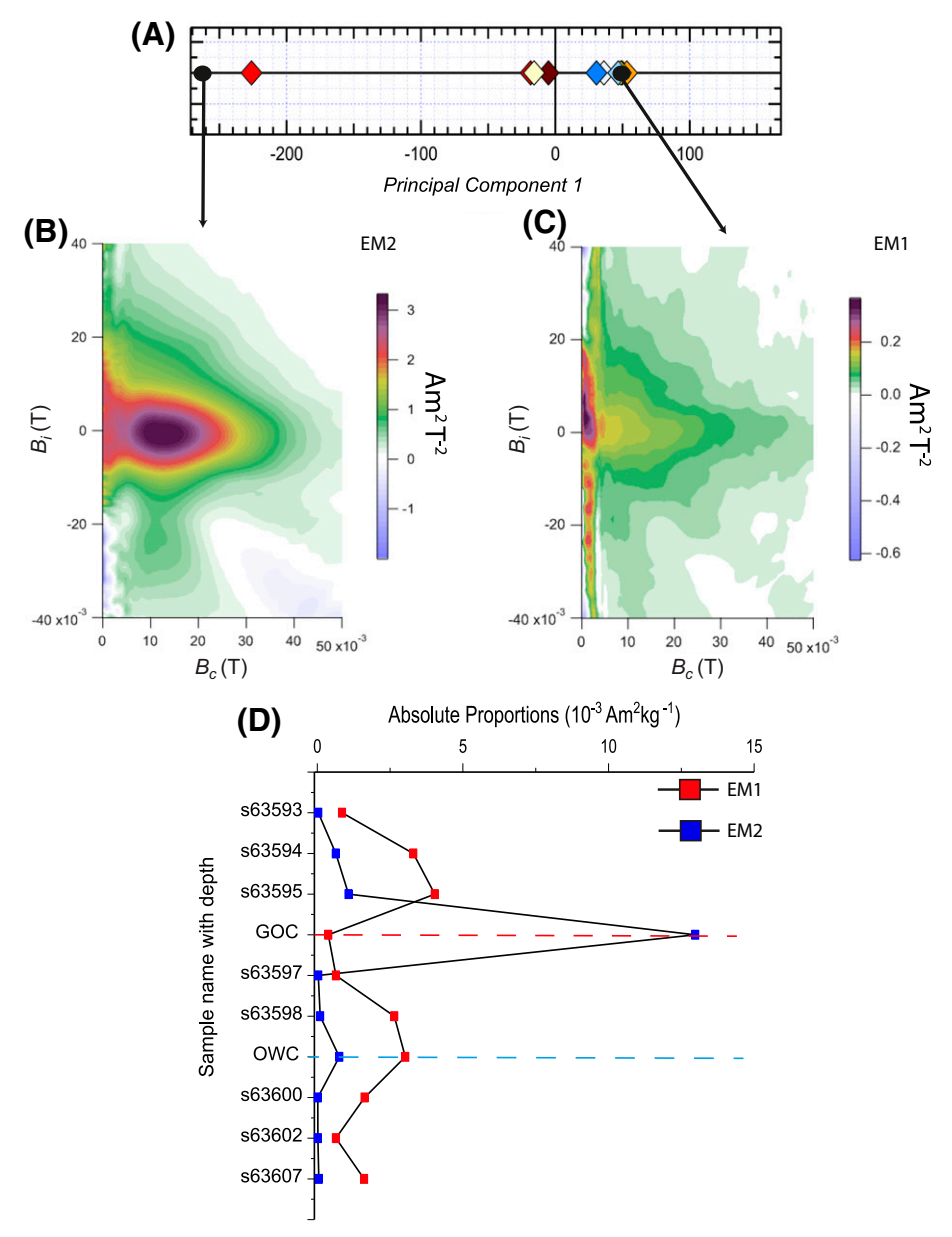


Figure 10. First-order reversal curve principal component analysis (FORC PCA) for well 21/25-04. (A) Principal component space, (B) end member 2 (EM2) represents single-domain particles with multiaxial anisotropy, (C) end member 1 represents superparamagnetic particles, and (D) proportions of end member 1 (EM1) and EM2 as a function of depth showing an increase in proportion of EM2 at the gas-oil contact (GOC) (red dashed line) and OWC (blue dashed line). The VARIFORC parameters (Egli, 2013) for FORC PCA smoothing are $s_{c,0} = 1.2$, $s_{c,1} = 3$, $s_{b,0} = 3$, $s_{b,1} = 5$, and $\lambda_c = 1$, $\lambda_b = 1$.

that the conditions in the reservoir can ensure the stability of greigite: a high concentration of reactive iron along with a low supply of organic carbon is needed to preserve greigite (Kao et al., 2004). Wells 21/25-04 and 21/25-A1 have API gravity ranging from 40° to 38°, which is indicative of sweet crude oil with low sulfur content and has been argued to prevent greigite from altering to pyrite (Wenger et al., 2002).

We suggest the thermodynamic stability diagrams in the reservoir includes a region for greigite between the pyrrhotite and pyrite regions (Sack and Ebel, 2006).

It is possible that subtle diagenetic changes in total dissolved sulfur, total dissolved iron, or total dissolved inorganic carbon at the top of the oil column and at the oil-water interface could favor the

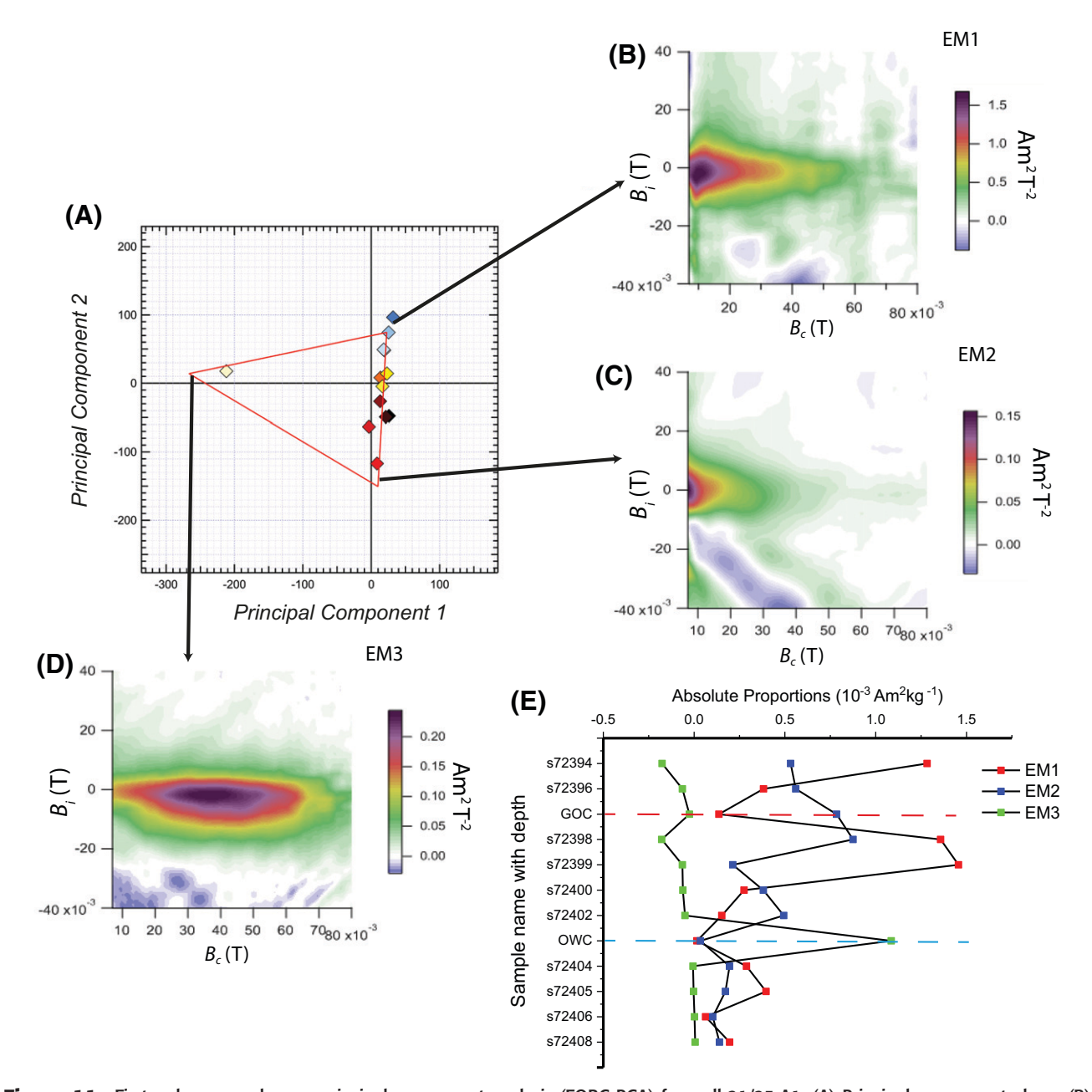


Figure 11. First-order reversal curve principal component analysis (FORC PCA) for well 21/25-A1. (A) Principal component plane, (B) end member 1 (EM1): superparamagnetic (SP) particles, (C) end member 2 (EM2): SP particles with multiaxial anisotropy, (D) end member 3 (EM3): stable single-domain greigite particles, and (E) proportions of EM1, EM2, and EM3 as a function of depth showing an increase in proportion of EM3 at the gas-oil contact (GOC) (red dashed line) and oil-water contact (OWC) (blue dashed line). The VARIFORC parameters (Egli, 2013) for FORC PCA smoothing are $s_{c,0} = 1.2$, $s_{c,1} = 3$, $s_{b,0} = 3$, $s_{b,1} = 5$, and $\lambda_c = 1$, $\lambda_b = 1$.

precipitation of SD greigite or magnetite at the hydrocarbon contacts. A model for the formation of magnetic minerals in the reservoir is shown in Figure 12. The SD grains are likely precipitated at the top of the oil column during early reservoir filling (Figure 12A). This continues until the spill point is reached and a stable OWC is formed, which kickstarts the formation of SD grains at the OWC (Figure 12B).

This continues as long as the trapping mechanism is unperturbed by geological processes (e.g., regional tilting, halokinesis, or compression). The reservoir receives a gas charge, the gas initially dissolves in the oil, and the precipitation of SD grains continues at the top of the oil column and at the OWC (Figure 12C). A change in pressure, temperature, or late gas charge results in the formation of a gas cap, which

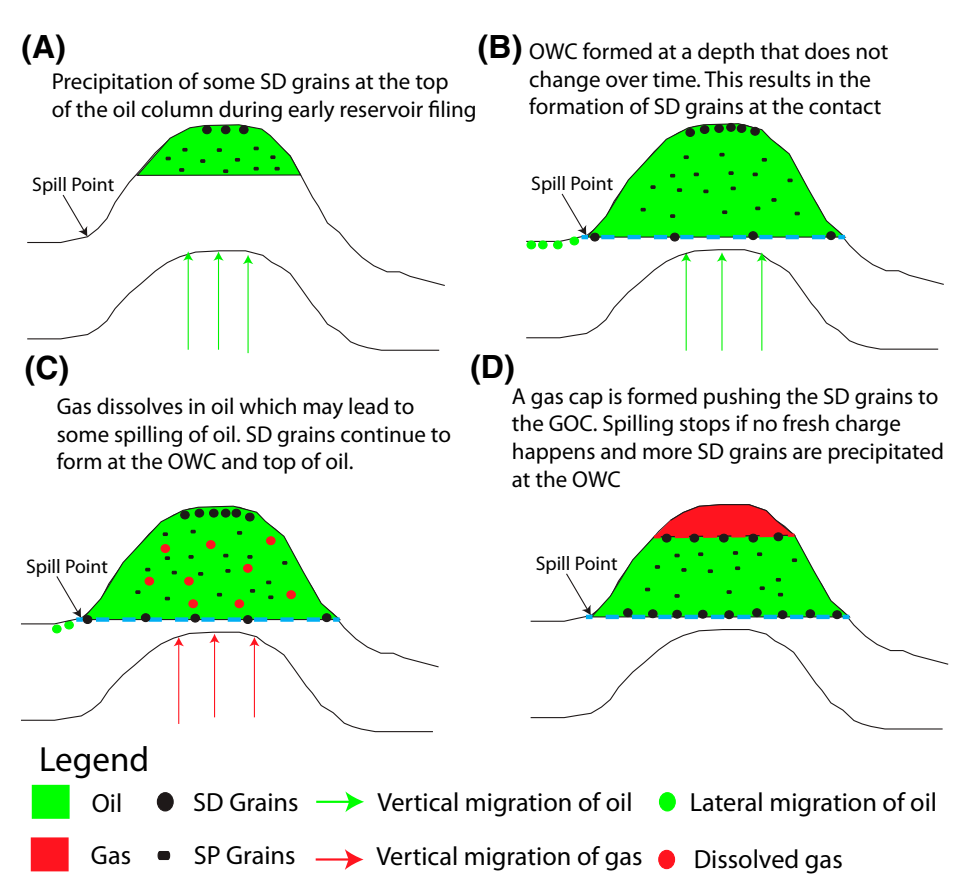


Figure 12. A schematic detailing the formation of single-domain (SD) grain at the gas-oil contact (GOC) and oil-water contact (OWC): (A) formation of SD grains at the top of the oil during early reservoir filling; (B) oil has filled to the spill point and the precipitation of SD grains occur at a stable OWC; (C) the reservoir is charged with gas, which dissolves in the oil, and the OWC is still stable, which results in continued precipitation of SD grains; and (D) a gas cap is formed pushing the SD grains formed at the top of the oil column to the GOC. SP = superparamagnetic.

displaces the oil and pushes the SD grains down the accumulation resulting in a concentration of SD grains at the GOC (Figure 12D).

Second, a biological mechanism: Biodegradation may be responsible for the precipitation of SD magnetic minerals at the hydrocarbon contacts. Biodegradation of hydrocarbons can occur during early reservoir filling or at the oil-water interface in temperatures less than 80°C (Head et al., 2003). Depending on the bacteria, SD magnetite or greigite may be produced. Bacteria such as GS-15 can produce fine grained extracellular magnetite via oxidation of certain hydrocarbons in an anaerobic environment, whereas sulfate reducing bacteria such as prokaryotes generate high concentrations of hydrogen sulfide, which combines with iron to produce fine-grained greigite (Mann et al., 1990). Wells 21/ 25-04 and 21/25-A1 are interpreted to have been cooler than 80°C at the onset of reservoir filling before rapid burial caused an increase in temperature (Badejo et al., 2020). It is possible that limited biodegradation would have occurred at the top of the oil column during trap filling and at the OWC resulting in precipitation of SD magnetite or greigite at the contacts prior to burial.

A schematic showing the variation of grain sizes of magnetic minerals precipitated by the diagenetic environment caused by hydrocarbons is shown in Figure 13. This observation could be used to identify both the OWC and GOC when conventional methods are unreliable. Given most of the magnetic minerals should remain in the host rock after hydrocarbon leakage, this technique has the potential to identify paleo-hydrocarbon contacts: either flat or tilted because of structuration. Identification of paleohydrocarbon contacts can provide information on the filling history of a series of fields within a basin, which can help calibrate petroleum systems models.

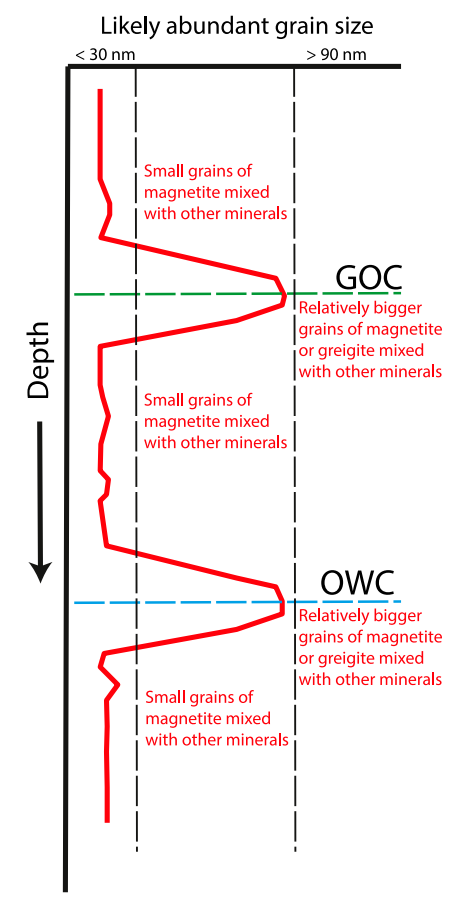


Figure 13. A schematic of the authigenic ferromagnetic magnetic mineral grain sizes as a function of depth within the reservoir. GOC = gas-oil contact; OWC = oil-water contact.

CONCLUSIONS

Peaks in measured magnetic susceptibility, M_s , and saturation remanent magnetization values have been observed at both the GOC and OWC in Tay Sandstone Member oil fields (Figure 6). Detailed magnetic analysis showed these peaks to be caused by an increase in the proportion of SD magnetite or greigite at the hydrocarbon-fluid contacts (Figures 10, 11, 13). Subtle diagenetic changes at the top of the oil column and at the oil-water interface are likely to be responsible for the observed anomalies at the GOC and OWC (Figure 12). Biodegradation during early filling of the reservoir and at the OWC may also be the direct cause of or enhancement of the signal at the hydrocarbon-fluid contacts. Our understanding of the processes at contacts are currently being refined as part of a new study at Imperial College London. This observation is of importance to the oil industry. because the presence

hydrocarbon-fluid contacts can be identified by carrying out quick magnetic susceptibility measurements on whole core samples from dry wells. This would give information on the filling history of a basin, for example, through identifying a paleo-OWC or could be used in the calibration of petroleum systems models in both frontier and mature basins. This new method can importantly be used on core samples from hydrocarbon wells where conventional methods failed to identify the GOC or OWC.

REFERENCES CITED

Abubakar, R., A. R. Muxworthy, A. Fraser, M. A. Sephton, J. S. Watson, D. Heslop, G. A. Paterson, and P. Southern, 2020, Mapping hydrocarbon charge-points in the Wessex Basin using seismic, geochemistry and mineral magnetics: Marine and Petroleum Geology, v. 111, p. 510–528, doi:10.1016/j.marpetgeo.2019.08.042.

Abubakar, R., A. R. Muxworthy, M. A. Sephton, P. Southern, J. S. Watson, A. J. Fraser, and T. P. Almeida, 2015, Formation of magnetic minerals in hydrocarbon-generation conditions: Marine and Petroleum Geology, v. 68, Pt. A, p. 509–519.

Ahmed, T. H., 1989, Hydrocarbon phase behavior: Houston, Texas, Gulf Pub. Co., 424 p.

Aldana, M., V. Costanzo-Alvarez, and M. Díaz, 2003, Magnetic and mineralogical studies to characterize oil reservoirs in Venezuela: Leading Edge, v. 22, no. 6, p. 526–529, doi:10.1190/1.1587674.

Badejo, S., A. J. Fraser, M. Neumaier, and A. R. Muxworthy, in press, 3D petroleum systems modelling as an exploration tool in mature basins: A case study from the Central North Sea, UK: Marine and Petroleum Geology.

Besnus, M., and A. Meyer, 1964, Nouvelles données expérimentales sur le magnétisme de la pyrrhotine naturelle, *in* Proceedings of the International Conference on Magnetism, Nottingham, United Kingdom, September 7–11, 1964, v. 20, p. 507–511.

Burton, E. A., H. G. Machel, and J. Qi, 1993, Thermodynamic constraints on anomalous magnetization in shallow and deep hydrocarbon seepage environments *in* D. M. Aïssaoui, D. F. McNeill, and N. F. Hurley, eds., Applications of paleomagnetism to sedimentary geology: Tulsa, Oklahoma, SEPM Special Publication 49, p. 193–207.

Cayley, G., 1987, Hydrocarbon migration in the central North Sea, *in* J. Brooks and K. Glennie, eds., Petroleum geology of north west Europe: Graham and Trotman: London, Graham & Trotman, p. 549–555.

Chang, L., A. P. Roberts, Y. Tang, B. D. Rainford, A. R. Muxworthy, and Q. Chen, 2008, Fundamental magnetic parameters from pure synthetic greigite (Fe₃S₄): Journal of Geophysical Research: Solid Earth, v. 113, no. B6, 16 p.

Costanzo-Alvarez, V., M. Aldana, O. Aristeguieta, M. C. Marcano, and E. Aconcha, 2000, Study of magnetic

- contrasts in the Guafita oil field (south-western Venezuela): Physics and Chemistry of the Earth Part A: Solid Earth and Geodesy, v. 25, no. 5, p. 437–445, doi:10.1016/S1464-1895(00)00068-5.
- Dekkers, M. J., H. F. Passier, and M. A. A. Schoonen, 2000, Magnetic properties of hydrothermally synthesized greigite (F3S4) II. High- and low-temperature characteristics: Geophysical Journal International, v. 141, no. 3, p. 809–819, doi:10.1046/j.1365-246x.2000.00129.x.
- Dennis, H., J. Baillie, T. Holt, and D. Wessel-Berg, 2000, Hydrodynamic activity and tilted oil-water contacts in the North Sea: Oslo, Norway, Norwegian Petroleum Society Special Publication 9, p. 171–185, doi:10.1016/S0928-8937(00)80016-8.
- Dunlop, D. J., and O. Ozdemir 1997, Rock magnetism: Fundamentals and frontiers: Cambridge, United Kingdom, Cambridge University Press, 573 p.
- Egli, R., 2013, VARIFORC: An optimized protocol for calculating non-regular first-order reversal curve (FORC) diagrams: Global and Planetary Change, v. 110, p. 302–320, doi:10.1016/j.gloplacha.2013.08.003.
- Emmerton, S., A. R. Muxworthy, and M. A. Sephton, 2012, Magnetic characterization of oil sands at Osmington Mills and Mupe Bay, Wessex Basin, UK, *in* D. Elmore, A. R. Muxworthy, M. Mena, and M. Maldana eds., Remagnetization and chemical alteration of sedimentary rocks: Geological Society, London, Special Publications 2012, v. 371, p. 189–198, doi:10.1144/SP371.6.
- Erratt, D., G. M. Thomas, and G. R. T. Wall 1999, The evolution of the Central North Sea Rift: Geological Society, London, Petroleum Geology Conference Series, v. 5, p. 63–82.
- Frederichs, T., T. von Dobeneck, U. Bleil, and M. J. Dekkers, 2003, Towards the identification of siderite, rhodochrosite, and vivianite in sediments by their low-temperature magnetic properties: Physics and Chemistry of the Earth, v. 28, p. 669–679.
- Harrison, R. J., and J. M. Feinberg, 2008, FORCinel: An improved algorithm for calculating first-order reversal curve distributions using locally weighted regression smoothing: Geochemistry, Geophysics, Geosystems, v. 9, no. 5, 11 p., doi:10.1029/2008GC001987.
- Harrison, R. J., J. Muraszko, D. Heslop, I. Lascu, A. R. Muxworthy, and A. P. Roberts, 2018, An improved algorithm for unmixing first-order reversal curve diagrams using principal component analysis: Geochemistry, Geophysics, Geosystems, v. 19, no. 5, p. 1595–1610, doi:10.1029/2018GC007511.
- Head, I. M., D. M. Jones, and S. R. Larter, 2003, Biological activity in the deep subsurface and the origin of heavy oil: Nature, v. 426, no. 6964, p. 344–352, doi:10.1038/ nature02134.
- Horng, C.-S., 2018, Unusual magnetic properties of sedimentary pyrrhotite in methane seepage sediments: Comparison with metamorphic pyrrhotite and sedimentary greigite: Journal of Geophysical Research: Solid Earth, v. 123, no. 6, p. 4601–4617, doi:10.1002/2017JB015262.
- Horng, C.-S., and A. P. Roberts, 2018, The low-temperature Besnus magnetic transition: Signals due to monoclinic

- and hexagonal pyrrhotite: Geochemistry, Geophysics, Geosystems, v. 19, no. 9, p. 3364–3375, doi:10.1029/2017GC007394.
- Housen, B. A., S. K. Banerjee, and B. M. Moskowitz, 1996, Low-temperature magnetic properties of siderite and magnetite in marine sediments: Geophysical Research Letters, v. 23, no. 20, p. 2843–2846, doi:10.1029/ 96GL01197.
- Isaksen, G. H., 2004, Central North Sea hydrocarbon systems: Generation, migration, entrapment, and thermal degradation of oil and gas: AAPG Bulletin, v. 88, no. 11, p. 1545–1572, doi:10.1306/06300403048.
- Kao, S.-J., C.-S. Horng, A. P. Roberts, and K.-K. Liu, 2004, Carbon–sulfur–iron relationships in sedimentary rocks from southwestern Taiwan: Influence of geochemical environment on greigite and pyrrhotite formation: Chemical Geology, v. 203, no. 1–2, p. 153–168, doi:10. 1016/j.chemgeo.2003.09.007.
- Kind, J., I. García-Rubio, M. Charilaou, N. R. Nowaczyk, J. F. Löffler, and A. U. Gehring, 2013, Domain-wall dynamics in 4C pyrrhotite at low temperature: Geophysical Journal International, v. 195, no. 1, p. 192–199, doi:10.1093/ gji/ggt262.
- Kubala, M., M. Bastow, S. Thompson, I. Scotchman, and K. Oygard, 2003, Geothermal regime, petroleum generation and migration, in D. Evans, C. Graham, A. Armour, and P. Bathurst, eds., The millennium atlas: Petroleum geology of the central and northern North Sea: London, Geological Society of London, chap. 17, p. 17-1–17-25.
- Larter, S., and R. di Primio, 2005, Effects of biodegradation on oil and gas field PVT properties and the origin of oil rimmed gas accumulations: Organic Geochemistry, v. 36, no. 2, p. 299–310, doi:10.1016/j.orggeochem.2004. 07.015.
- Lascu, I., J. F. Einsle, M. R. Ball, and R. J. Harrison, 2018, The vortex state in geologic materials: A micromagnetic perspective: Journal of Geophysical Research: Solid Earth, v. 123, no. 9, p. 7285–7304, doi:10.1029/2018JB015909.
- Lin, Q., J. Wang, T. J. Algeo, F. Sun, and R. Lin, 2016, Enhanced framboidal pyrite formation related to anaerobic oxidation of methane in the sulfate-methane transition zone of the northern South China Sea: Marine Geology, v. 379, p. 100–108, doi:10.1016/j.margeo. 2016.05.016.
- Liu, Q., Q. Liu, L. Chan, T. Yang, X. Xia, and T. Cheng, 2006, Magnetic enhancement caused by hydrocarbon migration in the Mawangmiao Oil Field, Jianghan Basin, China: Journal of Petroleum Science Engineering, v. 53, no. 1–2, p. 25–33, doi:10.1016/j.petrol.2006.01.010.
- Machel, H. G., 1995, Magnetic mineral assemblages and magnetic contrasts in diagenetic environments With implications for studies of palaeomagnetism, hydrocarbon migration and exploration, in P. Turner and A. Turner, eds., Palaeomagnetic applications in hydrocarbon exploration and production, Geological Society, London, Special Publications 1995, v. 98, p. 9–29, doi:10.1144/GSL. SP.1995.098.01.02.
- Mann, S., N. H. C. Sparks, R. B. Frankel, D. A. Bazylinski, and H. W. Jannasch, 1990, Biomineralization of

- ferrimagnetic greigite (Fe_3S_4) and iron pyrite (FeS_2) in a magnetotactic bacterium: Nature, v. 343, no. 6255, p. 258–261, doi:10.1038/343258a0.
- Mena, M., and A. M. Walther, 2012, Rock magnetic properties of drill cutting from a hydrocarbon exploratory well and their relationship to hydrocarbon presence and petrophysical properties: Geological Society, London, Special Publications 2012, v. 371, p. 217–228, doi:10.1144/SP371.14.
- Morin, F. J., 1950, Magnetic susceptibility of αFe_2O_3 and αFe_2O_3 with added titanium: Physical Review, v. 78, p. 819–820, doi:10.1103/PhysRev.78.819.2.
- Muxworthy, A. R., 2001, Effect of grain interactions on the frequency dependence of magnetic susceptibility: Geophysical Journal International, v. 144, no. 2, p. 441–447, doi:10.1046/j.1365-246x.2001.00342.x.
- Nelson, P. H., 2009, Pore-throat sizes in sandstones, tight sandstones, and shales: AAPG Bulletin, v. 93, no. 3, p. 329–340, doi:10.1306/10240808059.
- Reynolds, R. L., N. S. Fishman, R. B. Wanty, and M. B. Goldhaber, 1990, Iron sulfide minerals at Cement oil field, Oklahoma: Implications for magnetic detection of oil fields: Geological Society of America Bulletin, v. 102, no. 3, p. 368–380, doi:10.1130/0016-7606(1990)102<0368: ISMACO>2.3.CO;2.
- Rider, M. H., and M. Kennedy, 1996, The geological interpretation of well logs: Aberdeen, United Kingdom, Rider-French, 440 p.
- Roberts, A. P., 2015, Magnetic mineral diagenesis: Earth-Science Reviews, v. 151, p. 1–47, doi:10.1016/j.earscirev. 2015.09.010.
- Roberts, A. P., T. P. Almeida, N. S. Church, R. J. Harrison, D. Heslop, Y. Li, J. Li, A. R. Muxworthy, W. Williams, and X. Zhao, 2017, Resolving the origin of pseudo-single domain magnetic behavior: Journal of Geophysical Research: Solid Earth, v. 122, no. 12, p. 9534–9558, doi:10.1002/2017JB014860.
- Roberts, A. P., D. Heslop, X. Zhao, and C. R. Pike, 2014, Understanding fine magnetic particle systems through use of first-order reversal curve diagrams: Reviews of Geophysics, v. 52, no. 4, p. 557–602, doi:10.1002/2014RG000462.
- Roberts, A. P., C. R. Pike, and K. L. Verosub, 2000, First-order reversal curve diagrams: A new tool for characterizing the magnetic properties of natural samples: Journal of

- Geophysical Research: Solid Earth, v. 105, no. B12, p. 28461–28475, doi:10.1029/2000JB900326.
- Roberts, A. P., X. Zhao, R. J. Harrison, D. Heslop, A. R. Muxworthy, C. J. Rowan, J.-C. Larrasoaña, and F. Florindo, 2018, Signatures of reductive magnetic mineral diagenesis from unmixing of first-order reversal curves: Journal of Geophysical Research: Solid Earth, v. 123, no. 6, p. 4500–4522, doi:10.1029/2018JB015706.
- Sack, R. O., and D. S. Ebel, 2006, Thermochemistry of sulfide mineral solutions: Reviews in Mineralogy and Geochemistry, v. 61, no. 1, p. 265–364, doi:10.2138/rmg.2006.61.6.
- Sprain, C. J., J. M. Feinberg, P. R. Renne, and M. Jackson, 2016, Importance of titanohematite in detrital remanent magnetizations of strata spanning the Cretaceous-Paleogene boundary, Hell Creek region, Montana: Geochemistry, Geophysics, Geosystems, v. 17, no. 3, p. 660–678, doi:10.1002/2015GC006191.
- Valdez-Grijalva, M. A., and A. R. Muxworthy, 2019, First-order reversal curve (FORC) diagrams of nanomagnets with cubic magnetocrystalline anisotropy: A numerical approach: Journal of Magnetism and Magnetic Materials, v. 471, p. 359–364, doi:10.1016/j.jmmm.2018.09.086.
- Valdez-Grijalva, M. A., A. R. Muxworthy, W. Williams, P. Ó Conbhuí, L. Nagy, A. P. Roberts, and D. Heslop, 2018, Magnetic vortex effects on first-order reversal curve (FORC) diagrams for greigite dispersions: Earth and Planetary Science Letters, v. 501, p. 103–111, doi:10. 1016/j.epsl.2018.08.027.
- Verwey, E. J. W., 1939, Electronic conduction of magnetite (Fe₃O₄) and its transition point at low temperatures: Nature, v. 144, no. 3642, p. 327–328, doi:10.1038/144327b0.
- Wenger, L. M., C. L. Davis, and G. H. Isaksen, 2002, Multiple controls on petroleum biodegradation and impact on oil quality: SPE Reservoir Evaluation & Engineering, v. 5, no. 5, p. 375–383.
- Wilkin, R. T., and H. L. Barnes, 1997, Formation processes of framboidal pyrite: Geochimica et Cosmochimica Acta, v. 61, no. 2, p. 323–339, doi:10.1016/S0016-7037 (96)00320-1.
- Zhao, X., D. Heslop, and A. P. Roberts, 2015, A protocol for variable-resolution first-order reversal curve measurements: Geochemistry, Geophysics, Geosystems, v. 16, no. 5, p. 1364–1377, doi:10.1002/2014GC005680.